# Nanoscale

Accepted Manuscript


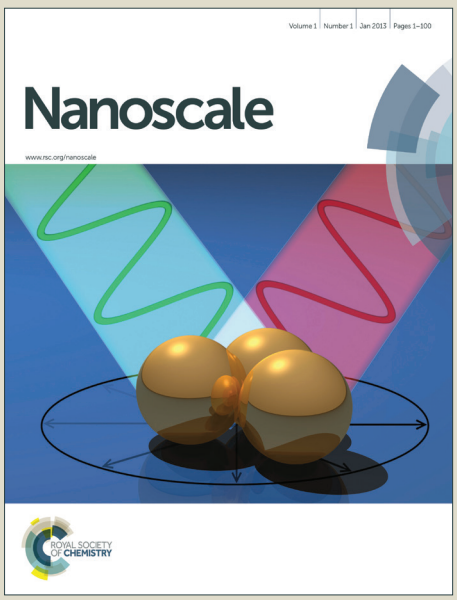





ROYAL SOCIETY OF CHEMISTRY

www.rsc.org/nanoscale

Cite this: DOI: 10.1039/c0xx00000x

www.rsc.org/xxxxxx

ARTICLE TYPE

# Alumina stabilized ZnO-graphene anode for lithium ion batteries via atomic layer deposition

**Mingpeng Yu[a], Aiji Wang[b], Yinshu Wang[b], Chun Li[a] and Gaoquan Shi*[a]**

***Received (in XXX, XXX) Xth XXXXXXXXX 20XX, Accepted Xth XXXXXXXXX 20XX***

**DOI: 10.1039/b000000x**

Atomic layer deposition (ALD) was applied to deposit ZnO on graphene aerogel, and this composite was used as an anode material for lithium ion batteries. This electrode material was further modified by an ultrathin $Al_2O_3$ layer via ALD to stabilize its electrochemical stability. These two metal oxides were uniformly immobilized on graphene frameworks, and the $Al_2O_3$ coating strongly improved the electrochemical performances of ZnO/graphene aerogel composite anodes. Particularly, the composite with a 10 ALD cycles of $Al_2O_3$ coating (denoted as ZnO-G-10) exhibited a high initial discharge capacity of 1513 mA h $g^{-1}$ and maintained a reversible capacity of 490 mA h $g^{-1}$ after 100 cycles at a current density of 100 mA $g^{-1}$. Furthermore, the capacity retention rate increased from 70% to 90% in comparison with its uncoated counterpart after 100 cycles. ZnO-G-10 anode also showed a good rate-capability, delivering a discharge capacity of 415 mA h $g^{-1}$ at 1000 mA $g^{-1}$. The improved electrochemical performance is attributed to the formation of an artificial solid electrolyte interphase layer, stabilizing ZnO and the electrolyte by preventing the aggregation of Zn/ZnO nanograins and the side reaction that would cause the degradation of anodes.

## Introduction

ZnO is a promising anode material for lithium ion batteries (LIBs) because of its high theoretical capacity of 987 mA h $g^{-1}$, which is nearly three times that of currently used graphite anode (theoretical capacity 372 mA h $g^{-1}$). Besides, ZnO is abundant, low cost and eco-friendly. ZnO can be facilely synthesized by a variety of techniques such as cathodic deposition,[1] hydrothermal synthesis,[2] and magnetron sputtering.[3] However, previous studies showed that ZnO electrodes suffer from severe capacity fading during long-term tests, even limited to dozens of cycling times.[4,5] This phenomenon was attributed to the severe volume change of electrode material that yields strong internal stress during alloy/dealloying cycles, leading to the pulverization of electrode material and subsequent the loss of its firm contact with the current collectors.[6]

ZnO displays redox reaction and alloy-dealloying chemistry similar to the Li insertion and extraction mechanism of $SnO_2$.[7,8] Upon a complete electrochemical lithium intercalation, the electrochemical processes are shown as follows:

$2xLi^+ + 2xe^- + MOx \rightarrow xLi_2O + M$; $x = 1$ or 2 for M = Zn or Sn

$yLi^+ + ye^- + M \rightarrow LiyM$; $y = 1$ or 4.4 for M = Zn or Sn

It should be noted that ZnO has an expansion coefficient of about 163% after lithium insertion, and this value is much lower than that of $SnO_2$ (300%).[1,9,10] Furthermore, the lithium-ion diffusion coefficient in ZnO is also higher than that in $SnO_2$.[11,12] However, pure ZnO exhibits much worse cycling performance compared with that of $SnO_2$.[4,7] A recent study revealed that the lithium embrittlement of ZnO is much more serious than that of $SnO_2$, leading to the electrochemically driven solid-state amorphization and pulverization of ZnO.[13] Besides, Zn nanograins migrate through the $Li_2O$ matrices faster than Sn nanoparticles during the volume variation; thus they aggregate much easier and faster.[4]

The performances of the metal oxide electrodes can be improved by several techniques. For example, decreasing the dimensions of metal oxide particles can shorten the diffusion lengths of $Li^+$ ions. The incorporation of carbonaceous materials can maintain the structural integrity and mitigate pulverization of oxides upon charging/discharging.[14–17] For these purposes, we previously fabricated a ZnO/graphene nanocomposites with an improved performance in LIBs using high energy ball milling.[18] However, this technique cannot reduce the particle sizes of oxides down to nanometre regime to form a uniform composite. The oxide particles were also tend to aggregate during the electrochemical alloy-dealloying process.[19] Furthermore, the oxide particles provided a large surface area for electrolyte-reduction reactions, leading inevitable capacity decay caused by the formation of solid-electrolyte-interphase (SEI) layer and the associated irreversible loss of Li. A recent study conducted by Wang *et al.* showed that even the particle size down to around

4 nm, $SnO_2$ still suffered serious pulverization and aggregation to form large particles.[9] Because the similarity between both oxides, ZnO would also exhibit the same behaviour.

SEI layer is an essential component of a battery. However, this layer usually suffers easy mechanical degradation and consumes active material.[9] To address this problem, a carbon layer was used to stabilize the SEI layer for againsting the fracture and deformation of electrode material. Carbon layer can also buffer the volume change of electrode and provide conductive paths for facile electron transport.[20,21] Surface modification of ZnO electrode with a carbon layer has been realized through various approaches, such as solvothermal method,[22] thermolysis[23] and carbonization of carbohydrates.[6] Unfortunately, in most cases, highly conformal and accurate controllable carbon coatings have not been achieved.

On the other hand, ALD can produce ultrathin oxide films with conformity much better than other available deposition techniques such as magnetron sputtering, pulsed laser deposition, and chemical vapour deposition. Additionally, the thicknesses of ALD films can be accurately controlled at angstrom level because of the unique self-limiting surface reactions. This technique is also cost-efficient because of the low costs of precursors. ALD technology allows exact and controllable modification of particle surfaces, enabling fine-tuning the physical, chemical and electrical properties of particles.[24,25] Actually, ALD has been widely applied to form ultrathin films for protecting the anode and cathode materials of batteries.[26–29]

In this work, we deposited nanoscale ZnO on the framework of a graphene aerogel via ALD process. Then, ultrathin $Al_2O_3$ coatings were further deposited onto the surfaces of ZnO-graphene nanocomposites with different ALD cycles. The $Al_2O_3$ stabilized ZnO/graphene composite anode exhibited excellent performances in LIBs including a high rate capability and cycling stability. A capacity of 415 mA h $g^{-1}$ was obtained at 1000 mA $g^{-1}$ for the ZnO-G-10 composite and this value is about 60% of the capacity delivered at 100 mA $g^{-1}$. Furthermore, the capacity fading was also greatly alleviated.

## Experimental Section

### Materials and methods

Graphene oxide (GO) was synthesized according to an improved Hummers method,[30] and it was used as the precursor of graphene hydrogel via a hydrothermal reduction process.[31] Typically, GO solution (3 mg $mL^{-1}$) was sealed in a Teflon-lined stainless-steel autoclave and treated at 180°C for 10 h. The product was washed with copious amounts of water and ethanol, and then freeze-dried to form a graphene aerogel. This highly porous morphology was favourable for the infiltration of the precursors of ZnO and guarantee the ZnO layer does not chock up the pores.

The procedures of preparing the $Al_2O_3$ coated ZnO/graphene composites are schematically illustrated in Fig. 1. ZnO layers were grown on the pore walls of graphene aerogel using $Zn(C_2H_5)_2$ and $H_2O$ as the reactants at 150°C for 60 ALD cycles. Then, the composite was treated by $Al_2O_3$-ALD for 0, 5, 10 and 20 cycles, respectively. Detailed procedures regarding the operation was provided in the Supporting information (ESI†). The resultant composites were designated as ZnO-G-$x$, $x$= 0, 5, 10 and 20, correspondingly.

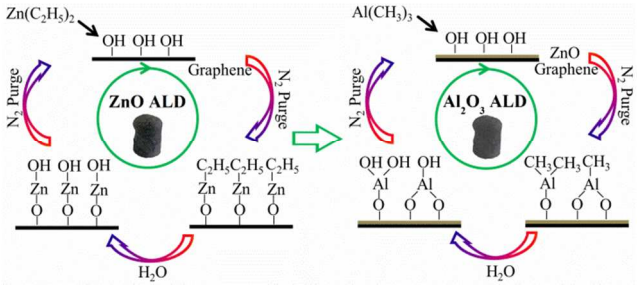


**Fig. 1** Schematic illustration of the ALD fabrication process.

### Characterizations

The crystalline structure of the composites were characterized by X-ray diffraction (XRD, PANanalytical) with Cu $K_\alpha$ radiation (λ= 1.5406 Å). Scanning transmission electron microscopy (STEM) and high resolution transmission electron microscopy (HRTEM) were performed on a Tecnai F20 instrument operated at 200 keV coupled with an energy dispersive X-ray spectrometer (EDS). Thermo gravimetric analysis (TGA) was carried out in air with a Perkin Elmer thermal analyzer at a heating rate of 10°C $min^{-1}$.

### Electrochemical Measurements

The ZnO-G-$x$ nanocomposite was mixed with polyvinyl difluoride (PVDF) binder with a weight ratio of 85:15 in 1-methyl-2-pyrrolidinone (NMP) solvent. The resultant slurry was then pasted on a copper foil and dried at 120°C for 12 h under vacuum. CR2032 coin cells were fabricated in an argon-filled glove box (MBraun, Unilab). The mass loading of electrode material was about 1.5 mg $cm^{-2}$. A lithium foil was used as both the counter and reference electrodes and a Celgard 2400 polypropylene membrane was used as the separator. The electrolyte was 1 M $LiPF_6$ in ethylene carbonate (EC)/dimethyl carbonate (DMC) (1:1 in volume). Galvanostatic charge/discharge cycles were tested using a Land CT-2001A (Wuhan, China) battery analyzer between 0.01 and 3 V (*vs.* $Li^+/Li$) and the capacities were calculated based on the weight of nanocomposites. Cyclic voltammograms (CV, 0.1 mV $s^{-1}$) tests were conducted on an electrochemical workstation (CHI 760D) under computer control.

## Result and Discussion

XRD patterns of the pure graphene aerogel (G-aerogel) and the composites are shown in Fig. 2a. In the pattern of G-aerogel, there is only a broad peak at about 2θ = 24.8°, which is consistent with our previous report.[31] After depositing 60 ALD cycles of ZnO, the composite exhibited diffraction peaks indexed as wurtzite-type hexagonal phase ZnO (space group P63mc, JCPDS No. 36-1451) with a crystallite size of 8.8 nm estimated by using the Scherrer's equation. This result is in a good agreement with that of the crystalline ZnO grown on graphene or Si substrate at low temperature.[32,33] After different cycles of depositing $Al_2O_3$, the overall features of these XRD patterns kept unchanged, suggesting the amorphous structures of $Al_2O_3$ coatings.

Each TGA curve in Fig. 2b shows a weight loss at around 500°C caused by the decomposition of graphene in air. Therefore, the ZnO content in the ZnO-G-0 composite was determined to be

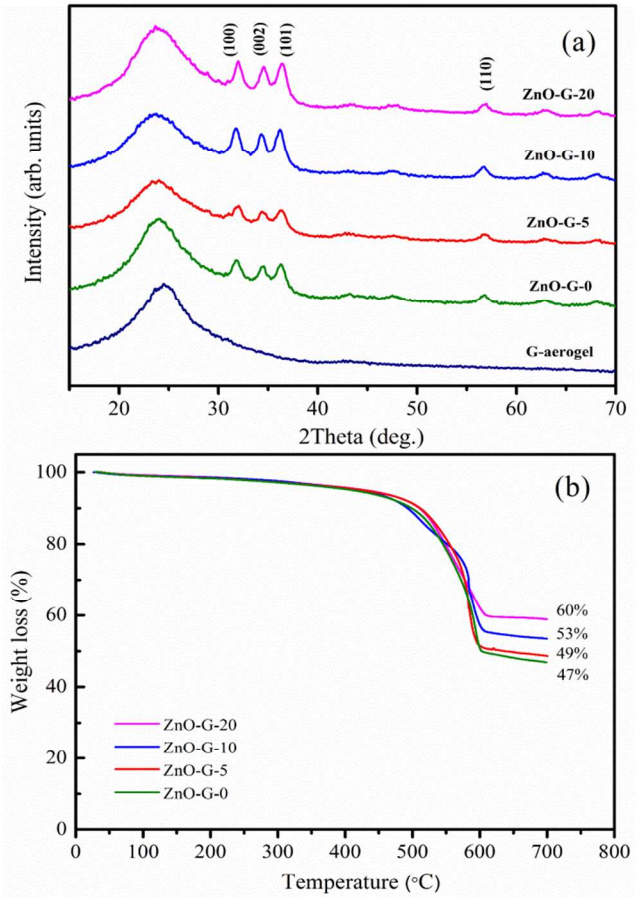


**Fig. 2** (a) XRD patterns of the graphene aerogel and the ZnO-G-$x$ composites and (b) TGA analysis of ZnO-G-$x$ composites.

about 47% after 60 ALD cycles. On the other hand, the weight percentages of the metal oxides (ZnO and $Al_2O_3$) in the ZnO-G-5, ZnO-G-10 and ZnO-G-20 composites were measured to be about 49%, 53% and 60%, respectively. The weight increment of the metal oxides in the composites was attributed to the $Al_2O_3$ layers coated on ZnO-G-0 composites.

The STEM image of the typical ZnO-G-10 composite indicates that ZnO nanoparticles formed by ALD are homogeneously anchored on graphene sheets (Fig. 3a). The other ZnO-G-$x$ composites exhibited similar morphologies (Figs. S1-S3 †). HRTEM image of a ZnO particle shows lattice fringes of its (100) crystal planes (inset of Fig. 3a). This image also reveals that an ultrathin and amorphous $Al_2O_3$ coating conformally enwraps around the crystalline ZnO nanograin. The thickness of $Al_2O_3$ coating is estimated to be about 1.2 nm, corresponding to an ALD growth rate of 1.2 Å per cycle.

EDS mapping results (Figs. 3b-3e) indicate the existence of aluminum and zinc elements in the composite; the corresponding signal intensities reveal their homogeneous distribution. It is reasonable to conclude that ZnO particles were nucleated at the widely distributed defect sites and remnant oxygen containing functional groups such as hydroxyl group of graphene sheets. The graphene framework worked like an elastic buffer to relieve the strain associated with the volume change during charging/charging processes to withstand the mechanical

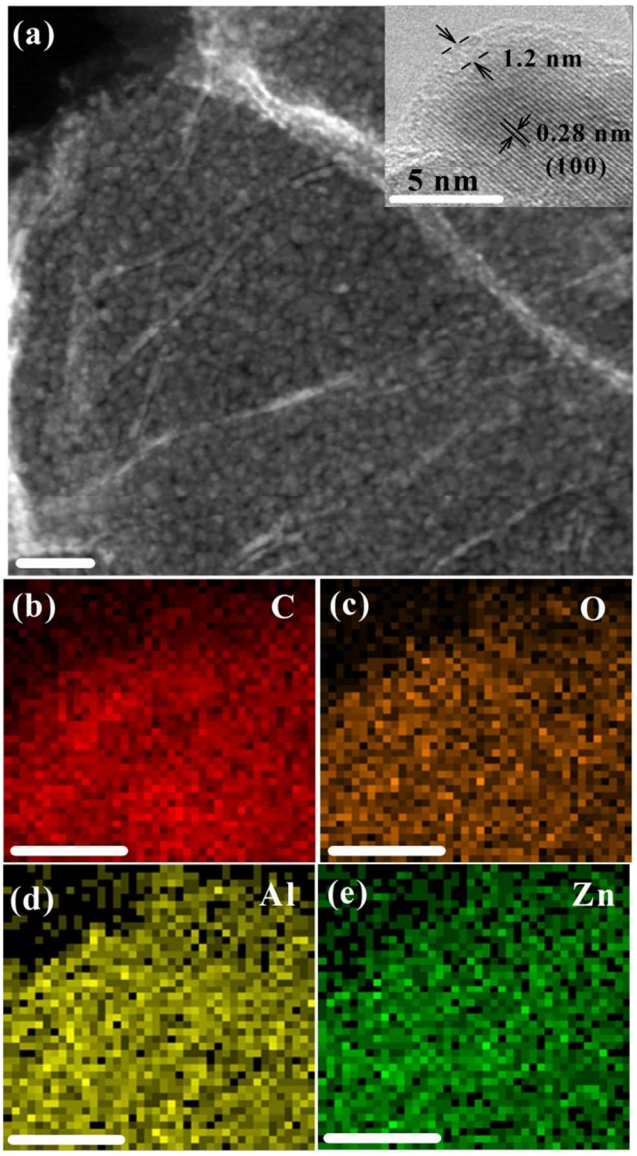


**Fig. 3** (a) STEM image of ZnO-G-10 nanocomposite and inset shows HRTEM image of ZnO nanograin coated with 10 $Al_2O_3$ ALD cycles, (b-e) Elemental mapping images of C, O, Al and Zn, (scale bars, 50 nm).

deformation of both contraction and expansion.

Fig. 4a shows the CV curves of the ZnO-G-10 nanocomposite electrode for the 1st, 2nd and 5th cycles in the potential range from 0 to 3.0 V (vs. $Li/Li^+$) at a scan rate of 0.1 mV $s^{-1}$. In the first cathodic scan, the broad peak centered around 0.3 V is related to a combination of several electrochemical reactions at close potentials, such as reducing ZnO with $Li^+$ to form Zn and $Li_2O$ and the alloying reaction between Li and Zn as well as the formation of the solid electrolyte interface (SEI) layer. The insertion of lithium into graphene can also be identified by the strong reduction peak at around 0.01 V. The corresponding anodic peaks between 0.2 to 0.7 V can be assigned to dealloying reactions of LiZn→ $Li_2Zn_3$→ $LiZn_2$→ $Li_2Zn_5$→ LiZn.[5,34]

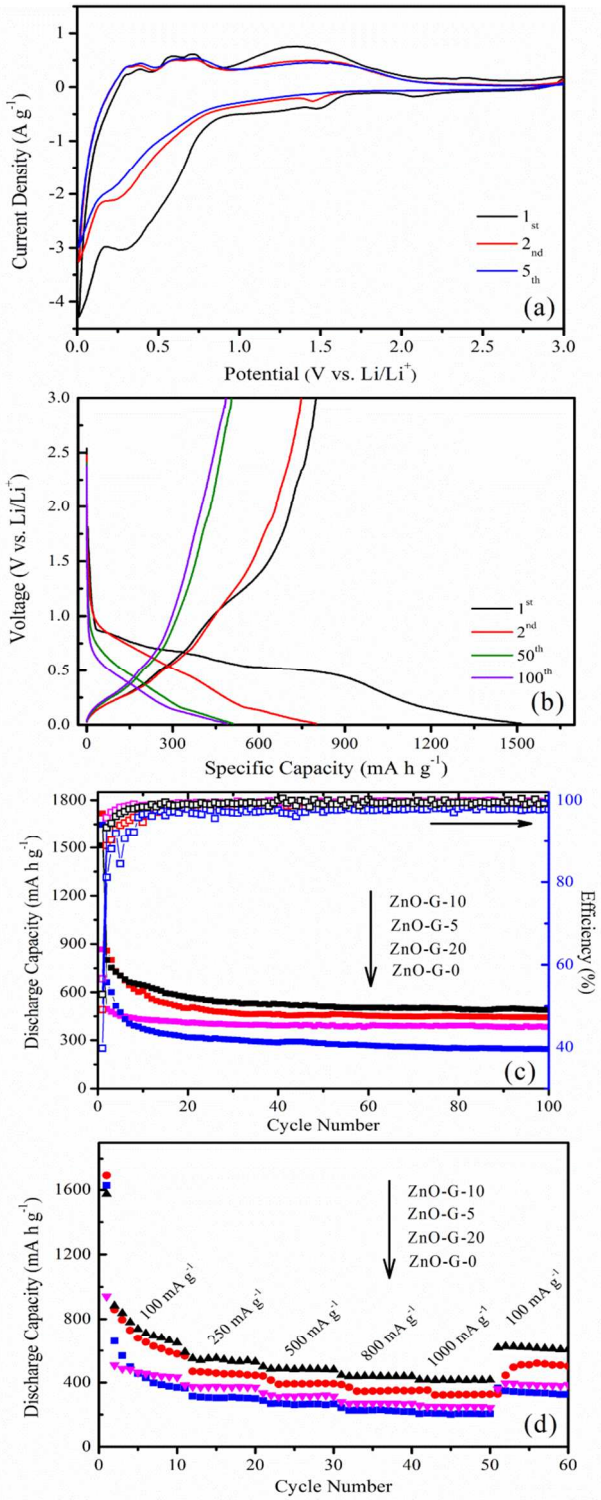


**Fig. 4** (a) cyclic voltammograms (CV) of ZnO-G-10 nanocomposite, (b) charge-discharge profiles at the 1st, 2nd, 50th, 100th cycles of ZnO-G-10 nanocomposite, (c) cycling performances (at 100 mA g$^{-1}$) and (d) rate performances (at 100 mA g$^{-1}$ to 1000 mA g$^{-1}$) of the ZnO-G-*x* nanocomposites with different $Al_2O_3$-ALD cycles.

Moreover, the broad peak around 1.4 V is related to the transformation of Zn metal to ZnO.[18] The CV curves recorded after 2 cycles are nearly coincide with each other, suggesting a good electrochemical reversibility.

The CV curves of the uncoated ZnO-G-0 (Fig. S4†) is similar to that of ZnO-G-10, indicating that the thin $Al_2O_3$ coating film has little influence on the reaction mechanism between ZnO with lithium. However, the current densities of CV waves decreased upon the increase in cycling number for ZnO-G-10 (Fig. 4a) is much weaker than that for ZnO-G-0 (Fig. S4†), indicating the stabilization of the anode by the protection of $Al_2O_3$-ALD layer.

The galvanostatic charge/discharge curves of the ZnO-G-10 composite electrode in the 1st, 2nd, 50th, and 100th cycles at 100 mA g$^{-1}$ are shown in Fig. 4b. The charge/discharge curves for the anodes coated with $Al_2O_3$ layers for different ALD cycles were similar to each other (Fig. 4b and Figs. S5–S7†). During the first discharge, a plateau appears at around 0.8 V for all electrodes, which is related to the conversion reaction between ZnO and Li, and the formation of SEI layer. While the following weak plateau is assigned to the generation of Li-Zn alloy and lithium ion intercalation into graphene. During charging, the voltage plateauses at around ~1.2 V are attributed to the oxidation reaction of Zn with $Li_2O$, in good agreement with the CV results.[35,36] From the second cycle onwards, the curves have similar shapes, implying the excellent electrochemically reversible reaction.

Fig. 4c shows long-term cycling behavior and the corresponding coulombic efficiencies of the $Al_2O_3$ coated and uncoated ZnO-G-0 nanocomposites at 100 mA h g$^{-1}$. For the $Al_2O_3$ coated electrodes, much more stable cycling performances were observed. This phenomenon can be explained by the stable chemical covalent bonding among $Al_2O_3$, ZnO and graphene, excellent electrical conductivity and good structural stability of the anode during long-term cycling. Furthermore, they also exhibited higher columbic efficiencies, indicating an improved reversible alloy/dealloying reaction of Li and Zn. These results also indicate that too much electrochemically inactive and insulating $Al_2O_3$ resulted in lowering discharge capacity. The corresponding discharge capacities, initial columbic efficiencies and capacity retentions of these composite electrodes are summarized in Table 1.

The initial irreversible capacity loss for each sample is possibly originated from the electrolyte decomposition in the low potential region and the formation of solid SEI layer. Another point worth mentioning is that, SEI formation is roughly linearly proportional to the specific surface area of carbonaceous materials.[37] The $Al_2O_3$ deposition further filled the pores and decreased the surface area of ZnO-G-0 composite, reducing the initial irreversible capacity loss accordingly.[38] $Al_2O_3$-ALD coating layer greatly increased the capacity of ZnO-G composite electrode. Specifically, ZnO-G-10 delivered a capacity of 490 mA h g$^{-1}$ after 100 cycles, which is about twice the capacity of pristine ZnO-G-0. The ZnO-G-10 anode exhibited exceptional electrochemical stability during the cycling process compared with those of other nanocomposites. The performances of ZnO-G-10 are among the best in the literature for ZnO based anodes (Table S1 in ESI†). The initial coulombic efficiency of

Cite this: DOI: 10.1039/c0xx00000x

www.rsc.org/xxxxxx

# ARTICLE TYPE

**Table 1** Discharge capacities ($C_{dis}$), reversible capacity retentions ($C_{ret} = C_{dis,100th}/C_{dis,2nd}$) and initial charge efficiencies (1st eff.) of ZnO-G-x electrodes measured at a current density of 100 mA $g^{-1}$.

| Sample | $C_{dis,1st}$ (mA h $g^{-1}$) | $C_{dis,2nd}$ (mA h $g^{-1}$) | $C_{dis,100th}$ (mA h $g^{-1}$) | $C_{ret}$ (%) | 1st eff. (%) |
|---|---|---|---|---|---|
| ZnO-G-0 | 1647 | 662 | 246 | 37.1 | 39.7 |
| ZnO-G-5 | 1717 | 859 | 443 | 51.5 | 49.1 |
| ZnO-G-10 | 1513 | 800 | 487 | 60.8 | 53.1 |
| ZnO-G-20 | 876 | 497 | 385 | 77.4 | 56.6 |

ZnO-G-20 composite is 56.6%, which is significantly higher than that of the pristine ZnO-G-0 composite (39.7%), showing a remarkable decrease in the irreversible capacity loss.

The uniform dispersion of the ZnO nanoparticles with a graphene buffering structure is beneficial to the high-rate electrochemical performance. The rate capabilities of all the electrodes were evaluated at various current densities (100–1000 mA $g^{-1}$, Fig. 4d). ZnO-G-10 electrode exhibits the best rate capability; it maintains about 415 mA h $g^{-1}$ at a high current density of 1000 mA h $g^{-1}$, and this value is about 70% of its discharge capacity at 100 mA h $g^{-1}$. This rate performance further reflected the stability improvement of ZnO-G-0 electrode by the protection of $Al_2O_3$ layer. It can also be inferred that 5-cycle $Al_2O_3$-ALD coating (about 0.6 nm thick) is not enough to guarantee the robustness of nanostructures of electrode material during cycling. Large volume expansion and contraction during the cycling process made SEI unstable, lowering the coulombic efficiency and cyclic capacity. The 10-cycle $Al_2O_3$-ALD coating was found to be the most effective protective layer to accommodate the volume change, exhibiting the best cycling stability and rate capability. Ultrathin $Al_2O_3$ film worked as an artificial solid electrolyte interphase (SEI) layer to prevent the chemical reaction between ZnO and the electrolyte, stabilizing the interface between the electrode and electrolyte. The $Al_2O_3$ coating layer could also hinder the formation of SEI and thus reduce the initial irreversible capacity loss. As discussed above, a thick $Al_2O_3$ layer acted as an insulator and hindered Li-ion diffusion.

The excellent electrochemical behavior of ZnO-G-10 anode can be attributed to a combination of several factors: (1) nanostructured ZnO can shorten $Li^+$ diffusion length to improve cyclability and rate capability; (2) graphene sheets provided a flexible, mechanically strong and electrically conductive network to accommodate the volume expansion of the ZnO nanoparticles during the charge/discharge processes as well as deliver electrons efficiently and smoothly to the electrodes; thus, a high rate capability was guaranteed; (3) the covalent bonding interactions between the infrastructure materials (i.e. graphene and ZnO) have an inherent stability against the agglomeration of nanoparticles during cycling; (4) ALD $Al_2O_3$ can form an artificial SEI layer to inhibit the detrimental chemical reaction between ZnO and the electrolyte by prohibiting their direct contacts.[9] These factors could have a synergetic effect on the electrochemical performances of $Al_2O_3$-ALD coated ZnO/graphene nanocomposites.

The morphological and structural changes of ZnO-G-0 or ZnO-G-10 electrode after charging/discharging at 100 mA h $g^{-1}$ for 100 cycles were studied by STEM and EDS mapping. In the case of ZnO-G-0 electrode, pulverized Zn/ZnO nanograins were aggregated into large particles with irregular shapes and sizes (Fig. 5a). In comparison, the Zn/ZnO nanograins in ZnO-G-10 electrode still maintained their initial ultrafine morphology with a highly uniform distribution, indicating the pulverization and aggregation of the anode material were suppressed during the long-term electrochemical cycling because of the protection of

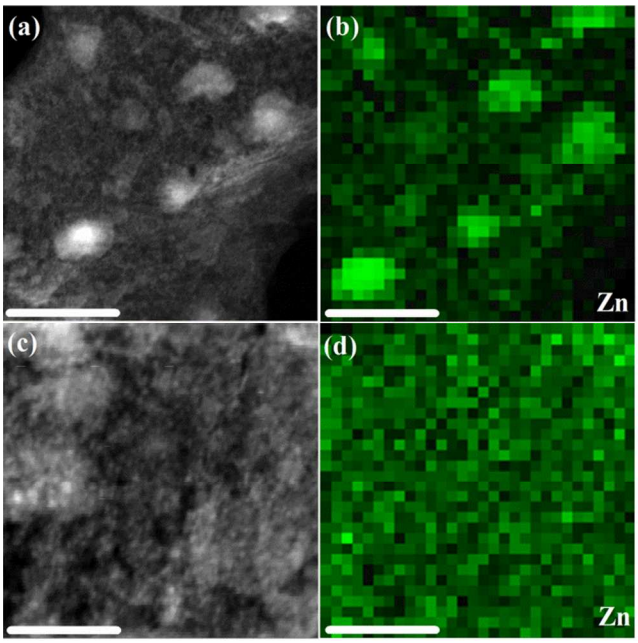


**Fig. 5** STEM and the EDS mapping images of (a, b) ZnO-G-0 and (c, d) ZnO-G-10 composites after 100 cycles of charging/discharging at 100 mA $g^{-1}$, (scale bars, 50 nm).

$Al_2O_3$ artificial SEI layer. Moreover, EDS mapping further verified the uniform distribution of Al element within the ZnO-G-10 electrode after 100 cycles (Fig. S8†). This result also reflected that the incorporation of an $Al_2O_3$ interface layer efficiently stabilized the ZnO/Zn nanograins and alleviated the volume variation of anode material during charging/discharging process. As a result, ZnO-G-10 electrode exhibited an improved electrochemical performance (Fig. 4).

## Conclusions

ZnO nanoparticles have been successfully anchored onto G-aerogel via ALD and the resulting composite was explored as an anode material of LIBs. The electrochemical performances of this electrode material can be greatly improved by an ultrathin ALD-$Al_2O_3$ coating. This is mainly due to that the $Al_2O_3$ coating acted as a physical protection layer and artificial ionic conductive SEI layer to maintain the mechanical integrity of ZnO-graphene electrode, preventing the aggregation of Zn/ZnO nanograins and inhibiting the direct contact between ZnO and electrolyte. This novel and robust $Al_2O_3$ wrapped ZnO-graphene architecture provided the electrode with a superior electrochemical performance in LIBs, including a high capacity, excellent rate capability and good cycling stability.

## Acknowledgements

This work was supported by the National Basic Research Program of China (973 Program, 2012CB933402, 2013CB933001), Natural Science Foundation of China (51161120361, 91027028) and the China Postdoctoral Science Foundation (2014M550708).

## Notes and references

[a]*Department of Chemistry, Tsinghua University, Beijing 100084, People's Republic of China. Fax: 86 62771149; Tel: 86 6277 3743; E-mail: gshi@tsinghua.edu.cn*
[b]*Department of Physics, Beijing Normal University, Beijing 100875, People's Republic of China.*

† Electronic Supplementary Information (ESI) available: [Procedures of ALD operation and supplementary figures]. See DOI: 10.1039/b000000x/

1 H. Wang, Q. Pan, Y. Cheng, J. Zhao, G. Yin, *Electrochim. Acta*, 2009, **54**, 2851-2855.
2 M. Ahmad, Y. Shi, A. Nisar, H. Sun, W. Shen, M. Wei, J. Zhu, *J. Mater. Chem.*, 2011, **21**, 7723–7729.
3 H. -Q. Dai, H. Xu, Y. -N. Zhou, F. Lu, Z. -W. Fu, *J. Phys. Chem. C*, 2011, **116,** 1519–1525.
4 P. A. Connor, F. Belliard, M. Behm, L. G. Tovar, J. T .S. Irvine, *Ionics*, 2002, **8**, 172–176.
5 F. Belliard, J.T.S. Irvine, *J. Power Sources*, 2001, **97-98,** 219–222.
6 J. Liu, Y. Li, R. Ding, J. Jiang, Y. Hu, X. Ji, Q. Chi, Z. Zhu, X. Huang, *J. Phys. Chem. C*, 2009, **113**, 5336–5339.
7 F. Belliard, P.A. Connor, J.T.S. Irvine, *Ionics*, 1999, **5,** 450–454.
8 H. Li, X. Huang, L. Chen, *Solid State Ionics*, 1999, **123**, 189–197.
9 D. Wang, J. Yang, J. Liu, X. Li, R. Li, M. Cai, T.-K. Sham, X. Sun, *J. Mater. Chem. A*, 2014, **2**, 2306–2312.
10 I. A. Courtney, J. Dahn, *J. Electrochem. Soc.*, 1997, **144**, 2045–2052.
11 J. Xie, N. Imanishi, A. Hirano, Y. Takeda, O. Yamamoto, X. B. Zhao, G. S. Cao, *Thin Solid Films*, 2011, **519,** 3373–3377.
12 J. Xie, N. Imanishi, A. Hirano, Y. Takeda, O. Yamamoto, X. B. Zhao, G. S. Cao, *Solid State Ionics*, 2010, **181,** 1611–1615.
13 A. Kushima, X.H. Liu, G. Zhu, Z. L. Wang, J. Y. Huang, J. Li, *Nano Lett.*, 2011, **11**, 4535–4541.
14 F. Sun, J. Wang, D. Long, W. Qiao, L. Ling, C. Lv, R. Cai, *J. Mater. Chem. A*, 2013, **1**, 13283–13289.
15 C.-T. Hsieh, C.-Y. Lin, Y.-F. Chen, J.-S. Lin, *Electrochim. Acta*, 2013, **111**, 359–365.
16 D. Wang, J. Yang, X. Li, D. Geng, R. Li, M. Cai, T.-K. Sham, X. Sun, *Energy Environ. Sci.*, 2013, **6**, 2900–2906.
17 C. Zhang, X. Peng, Z. Guo, C. Cai, Z. Chen, D. Wexler, S. Li, H. Liu, *Carbon*, 2012, **50,** 1897–1903.
18 M. Yu, D. Shao, F. Lu, X. Sun, H. Sun, T. Hu, G. Wang, S. Sawyer, H. Qiu, J. Lian, *Electrochem. Comm.*, 2013, **34**, 312–315.
19 N. Zhang, Q. Zhao, X. Han, J. Yang, J. Chen, *Nanoscale*, 2014, **6**, 2827–832.
20 D. Aurbach, M.D. Levi, E. Levi, A. Schechter, *J. Phys. Chem. B*, 1997, **101**, 2195–2206.
21 W. -M. Zhang, X.-L. Wu, J. -S. Hu, Y. -G. Guo, L.-J. Wan, *Adv. Funct. Mater.*, 2008, **18,** 3941–3946.
22 X. Shen, D. Mu, S. Chen, B. Wu, F. Wu, *ACS Appl. Mater. Interfaces*, 2013, **5**, 3118–3125.
23 M. M. Hossain, A. H. A. Mamun, J. R. Hahn, *J. Phys. Chem. C*, 2012, **116**, 23153–23159.
24 M. Liu, X. Li, S. K. Karuturi, A. I. Y. Tok, H. J. Fan, *Nanoscale*, 2012, **4**, 1522–1528.
25 J. Luo, J. Liu, Z. Zeng, C. F. Ng, L. Ma, H. Zhang, J. Lin, Z. Shen, H. J. Fan, *Nano lett.*, 2013, **13**, 6136–6143.
26 L. F. Hakim, J. Blackson, S. M. George, A. W. Weimer, *Chem. Vapor Depos.*, 2005, **11**, 420–425.
27 I. D. Scott, Y. S. Jung, A. S. Cavanagh, Y. Yan, A. C. Dillon, S. M. George, S. -H. Lee, *Nano Lett.*, 2010, **11**, 414–418.
28 X. Meng, X. -Q. Yang, X. Sun, *Adv. Mater.*, 2012, **24**, 3589–3615.
29 M. Yu, W. Yuan, C. Li, J.-D. Hong, G. Shi, *J. Mater. Chem. A*, 2014, **2**, 7360-7366.
30 J. Chen, B. Yao, C. Li, G. Shi, *Carbon*, 2013, **64**, 225–229.
31 Y. Xu, K. Sheng, C. Li, G. Shi, *ACS Nano*, 2010, **4**, 4324–4330.
32 X. Sun, C. Zhou, M. Xie, H. Sun, T. Hu, F. Lu, S. M. Scott, S. M. George, J. Lian, *J. Mater. Chem. A*, 2014, **2,** 7319–7326.
33 J. Malm, E. Sahramo, J. Perälä, T. Sajavaara, M. Karppinen, *Thin Solid Films*, 2011, **519,** 5319–5322.
34 J. Liu, Y. Li, X. Huang, G. Li, Z. Li, *Adv. Funct. Mater.*, 2008, **18**, 1448–1458.
35 Q. Xie, X. Zhang, X. Wu, H. Wu, X. Liu, G. Yue, Y. Yang, D. -L. Peng, *Electrochim. Acta*, 2014, **125**, 659–665.
36 C. Zhang, J. Tu, Y. Yuan, X. Huang, X. Chen, F. Mao, *J. Electrochem. Soc.*, 2007, **154**, A65–A69.
37 M. Winter, P. Novák, A. Monnier, *J. Electrochem. Soc.*, 1998, **145**, 428–436.
38 J. W. Elam, J. A. Libera, T. H. Huynh, H. Feng, M. J. Pellin, *J. Phys. Chem. C*, 2010, **114**, 17286–17292.